

3                   **Basement topography and sediment thickness beneath Antarctica's Ross Ice Shelf**4                   M.D. Tankersley<sup>1,2</sup>, H.J. Horgan<sup>1</sup>, C.S. Siddoway<sup>3</sup>, F. Caratori Tontini<sup>2,4</sup>, K.J. Tinto<sup>5</sup>5                   <sup>1</sup>Antarctic Research Centre, Victoria University of Wellington, Wellington, New Zealand6                   <sup>2</sup>GNS Science, Lower Hutt, New Zealand7                   <sup>3</sup>Colorado College, Colorado Springs, CO, USA8                   <sup>4</sup>University of Genova, Genova, Italy9                   <sup>5</sup>Lamont-Doherty Earth Observatory, Columbia University, Palisades, NY, USA10                  **Contents of this file**

11                  Text S1 to S7

12                  Table S1

13                  Figures S1 to S6

14                  **Introduction**

This supplement provides additional information on the assumptions behind the process of determining basement depth from magnetic anomalies (**Text S1**), the collection and processing of aeromagnetic line data (**Text S2**), the methodology of tying ROSETTA-Ice magnetic basement to ANTOSTRAT acoustic basement (Brancolini et al., 1995), through the use of Operation IceBridge (OIB) magnetic data (Cochran et al. 2014) (**Text S3 and S4**), the gridding, merging, and filtering of the resulting basement grid (**Text S5**), the calculation of sediment thickness and  $\beta$ -factors for the region (**Text S6**), and our quantification of uncertainties and comparison with points of previously measured sediment thickness (**Text S7**). Sediment thickness comparisons with past seismic surveys are included in **Table S1**. Also included are supplementary figures showing various additional Ross Ice Shelf grids (**Figure S1**), the Werner deconvolution solutions of OIB flight 403.3 (**Figure S2**), several selected ROSETTA-Ice flight lines with Werner deconvolution solutions (**Figure S3**), unfiltered basement solutions with flight line locations and individual Werner deconvolution solutions (**Figure S4**), uncertainties applied to basement and sediment thickness results (**Figure S5**), and misfit distributions between OIB, ANTOSTRAT, and ROSETTA basement models (**Figure S6**). Python code, within a Jupyter notebook, documents our workflow and figure creation and is accessible here: <https://zenodo.org/badge/latestdoi/470814953> or at the github repository: [https://github.com/mdtanker/RIS\\_basement\\_sediment](https://github.com/mdtanker/RIS_basement_sediment). Results in the form of netCDF's and csv's are available at <https://doi.pangaea.de/10.1594/PANGAEA.941238>, including figures of all ROSETTA-ice flight line basement solutions.

36 **Text S1. Depth to basement assumptions**

37 Our resulting basement grid is the depth to the shallowest magnetic signal. It is  
38 assumed that the crystalline basement in this region produces significantly larger  
39 magnetic anomalies compared to the overlying sediment fill. Note that in some  
40 instances, such as igneous bodies intruded into sedimentary basin fill, Werner-  
41 determined solutions fall upon the crest of the intrusion, and the actual top of the  
42 crystalline basement could be at a deeper level. Intrusions of small lateral extent will have  
43 small widths, resulting in small values of parameter S (susceptibility x width) and  
44 therefore will be removed by our filter (Text S3). For larger intrusions into existing basins,  
45 (i.e. Ross Island and Minna Bluff (Cox et al., 2019)), the modeled magnetic basement  
46 surface will be shallower than the bottom of the sedimentary basin. While this  
47 underestimates sediment volume, it better characterizes the competency of the substrate  
48 from an ice dynamics perspective. This is similar to how extensive intrusions into basins  
49 would be imaged by seismic surveys as shallow basement. However, these extensive  
50 regions of late-Cretaceous-Cenozoic magmatism are not expected to be prevalent under  
51 the RIS (Andrews et al., 2021).

52 **Text S2. Magnetic data collection, processing, and Werner deconvolution**

53 Both ROSETTA-Ice and OIB data sets were collected with a Scintrex CS3 Cesium  
54 magnetometer. Average flight speeds were 123 m/s and 93 m/s for OIB and ROSETTA-  
55 Ice respectively. Altitudes for the sections of OIB flight 403 used here average around  
56 400 m above sea level, while ROSETTA-Ice altitude averaged at 750 m above ground  
57 level. OIB data were resampled from 20Hz to 1Hz to match the frequency of the  
58 ROSETTA-Ice data. Both datasets have been despiked, diurnally corrected, and had the  
59 International Geomagnetic Reference Field model removed. See Tinto et al. (2019) for  
60 more details of the ROSETTA-Ice survey and flight line locations. Due to variable flight  
61 elevations, both between and within the datasets, all magnetic data were upward-  
62 continued to 1000 m above sea level. To avoid artefacts of downwards continuing, any  
63 data with flight elevations above 1000 m were removed (~10% of the data).

64 Here we use 2D Werner deconvolution (Werner, 1953), applied to aeromagnetic line  
65 data, to image the shallowest magnetic signals in the crust. Assuming that the overlying  
66 sediments produce smaller magnetic anomalies than the crystalline basement, we treat  
67 the resulting solutions as a depth to the magnetic basement. During Werner  
68 deconvolution, moving and expanding windows are passed over the magnetic anomaly  
69 line data. Within each window, after linearly detrending the data, the source parameters  
70 of the anomalies are estimated with a least-squares approach, assuming the source  
71 bodies are infinite-depth dikes or contacts. The source parameters include position  
72 (distance along profile and depth), magnetic susceptibility, and source geometry (contact  
73 or dike). Solutions are considered valid between 1200 m and 20 km of upward continued  
74 flight elevation (approx. 200 m - 19 km bsl). Windows ranged from 500 m - 50 km, with a  
75 window shift increment of 1 km and an expansion of 1 km.

76 Due to passing over the data many times with varying window widths, Werner  
77 deconvolution produces a depth-scatter of solutions, which tend to cluster vertically  
78 beneath the true magnetic sources. Each of these solutions consists of location, depth,  
79 susceptibility (S), window width (W), and a simplified source geometry (dike or contact).

80 For contact-type solutions, parameter S is the estimated magnetic susceptibility of the  
81 body, while for dike-type solutions, S is the product of susceptibility and dike width.  
82 During filtering (Text S3-4), a cut-off based on parameter S is used to remove shallow  
83 solutions. Since the value of parameter S for contact solutions are typically much smaller  
84 than for dike solutions (since they are not multiplied by dike width), only dike solutions  
85 have been considered here. To achieve a basement surface from this resulting depth-  
86 scatter of solutions, we have utilized parameter-based filtering and clustering, described  
87 in Text S3-4. This Werner deconvolution process was the same for both OIB and  
88 ROSETTA-Ice magnetics data. Werner deconvolution was performed in Geosoft's *Oasis*  
89 *Montaj* and subsequent processing of these results was performed in Python, and is  
90 included in a Jupyter notebook; <https://zenodo.org/badge/latestdoi/470814953>.

91 This magnetic basement approach has been used to map sedimentary basins  
92 throughout Antarctica, including the Ross Sea (Karner et al., 2005), western Marie Byrd  
93 Land (Bell et al., 2006), and Wilkes Subglacial Basin (Studinger et al., 2004; Frederick et al.,  
94 2016). Our approach is similar to past studies, but our proximity to well-constrained  
95 offshore seismic basement depths (Brancolini et al., 1995) allows us to develop the  
96 method further. Most studies display their results as 2D profiles with the depth-scatter of  
97 solutions mentioned above, and simply use the tops of the clusters as the basement  
98 depth. By comparison with seismic basement, we have developed a reliable, automated  
99 method of 'draping' a surface over these depth-scattered solutions to produce a 3D  
100 surface. This process is described below.

### 101 **Text S3. Tying magnetic basement to seismic basement**

102 To validate the method described in Text S2 and address uncertainty we perform  
103 Werner deconvolution for OIB magnetics data (Figure 1b, Cochran et al., 2014) over the  
104 Ross Sea. Here, ice-free conditions have permitted shipborne seismic surveys to image  
105 basement depths in the region. These have been compiled by the Antarctic Offshore  
106 Acoustic Stratigraphy project (ANTOSTRAT) (Brancolini et al., 1995) (Figure 1b). The  
107 basement was not imaged for the deeper portions of the basins and data coverage of  
108 actual basement reflectors, versus interpolation between basement reflectors, is not  
109 reported. Werner deconvolution (Text S2) produces a series of many solutions (black  
110 dots in Figures 2 & S2) at each window along the line.

111 To achieve a basement surface, instead of a depth-scatter of solutions, solutions  
112 were filtered based on Werner window width (W) and the product of magnetic  
113 susceptibility and body width (parameter S). Filtered solutions (black circles, scaled to  
114 parameter S in Figures 2 & S2) were then horizontally binned with variable bin sizes  
115 (parameter B) (vertical grey lines in Figures 2 & S2). Bins with a minimum count of  
116 solutions (parameter C) were retained, and the depth of the bin center was set to the  
117 95<sup>th</sup>-percentile depth of the solutions in the bin. This removed spurious shallow  
118 solutions, while effectively retaining the 'top' of the magnetic signal. These bin centers  
119 (orange crosses in Figures 2 & S2) were then interpolated, producing our model of  
120 magnetic basement depths (orange line in Figures 2 & S2). The above filtering  
121 techniques removed the solutions above the basement, and the clustering technique  
122 fitted a surface over the remaining points, which represents the top of the basement.

123 This interpolated line allowed a direct comparison between ANTOSTRAT seismic  
124 basement and OIB magnetic basement.

125 We varied each of the four parameters (W, S, B, and C) with 21 different values and  
126 conducted the above procedures for all unique combinations of them on OIB line 403,  
127 segments 1 and 3, in the Ross Sea (location in Figure 1b). This resulted in 194,481  
128 iterations, for each of which we calculated a mean absolute difference at points every  
129 5km between ANTOSTRAT seismic basement and the resulting OIB magnetic basement.  
130 We found the parameter values which produced the closest match between OIB  
131 magnetic basement and ANTOSTRAT seismic basement, as shown in Figures 2 & S2.  
132 These resulting values were a maximum Werner deconvolution window width (parameter  
133 W) of 10 km, a minimum product of magnetic susceptibility and body width (parameter  
134 S) of 1.0, a horizontal bin width (parameter B) of 36 km, and a minimum number of  
135 solutions per bin (parameter C) of 6. The median absolute misfit between OIB and  
136 ANTOSTRAT basement for the two line-segments was 480m (260m for Line 403.1 (Figure  
137 2), and 1040m for Line 403.3 (Figure S2)). This equates to 11% of average ANTOSTRAT  
138 depths for the two lines. The close fit between the OIB magnetic basement and the  
139 ANTOSTRAT seismic basement both supports the validity of this method and gives us  
140 the parameters necessary to repeat this method for data over the RIS.

#### 141 **Text S4. Tying Ross Sea magnetic basement to Ross Ice Shelf magnetic basement**

142 Having optimized our method to match OIB magnetic basement to ANTOSTRAT  
143 seismic basement in the Ross Sea (Text S3, Figures 2 & S2), we now optimize the method  
144 to match ROSETTA-Ice magnetic basement to OIB magnetic basement. This additional  
145 optimization is necessary due to differences in processing and survey design, including  
146 flight elevations, speed, aircraft, mounting equipment used, and frequency of recording.  
147 With the optimized parameters for OIB data (Text S3), we calculate magnetic basement  
148 for OIB flight 404 over the ice shelf. We treat this as the 'true' basement and update the  
149 filtering and clustering parameters (Text S2) to minimize the misfit between OIB  
150 basement and the resulting ROSETTA-Ice basement. This tuning was performed on  
151 ROSETTA-Ice lines 590 and 650, which were coincident with segments from OIB line 404  
152 (location in Figures 1b & S4). Optimal parameters to match ROSETTA-Ice solutions to  
153 OIB basement are found to be  $W < 26$  km,  $S > 1.2$ ,  $B = 36$  km, and  $C > 40$ , resulting in a  
154 median absolute misfit between OIB basement and ROSETTA-Ice solutions of 400 m  
155 (630m for line 404.590 (Figure S3e) and 310m for line 404.590 (Figure S3f)). This equates  
156 to 18% of OIB depths for the two lines. With these parameters which best match  
157 ROSETTA magnetic basement to OIB magnetic basement, we performed the same  
158 procedure on all the ROSETTA-ice flight lines. A selection of these lines, and the two ties  
159 to OIB 404, are shown in Figure S3. All ROSETTA-ice flight line solutions are available as  
160 images at the PANGAEA link.

#### 161 **Text S5. Gridding, merging, and filtering**

162 The above processes were performed on all ROSETTA-ice flight lines (white lines in  
163 Figure S4), including the N-S tie lines at ~55 km spacing. Where the tie lines crossed  
164 over the E-W flights lines, some resulting basement solutions (black dots in Figure S4)  
165 are nearby those from the crossing line. Since we are interested in the shallowest

166 magnetic signals, we have retained only the shallowest solution with 8km cells across our  
167 region. Since bin widths (parameter B) were set to 36 km, the nearest solutions along  
168 individual lines were further apart than the 8km cell. The closest spacing of E-W flight  
169 lines was 10 km, so this process only affected solutions at the crossover between N-S  
170 and E-W lines. These points were then gridded with a 5 km cell size and a minimum  
171 curvature spline with a tension factor of 0.35 (Smith & Wessel, 1990) (Figure S4). This  
172 grid was then merged with a Ross Sea seismic basement grid. The Ross Sea grid, while  
173 mostly ANTOSTRAT data, was sourced from a regional compilation of sediment  
174 thicknesses (Lindeque et al., 2016, Wilson and Luyendyk 2009), we have subtracted from  
175 bathymetry depths (Morlighem et al. 2020) to achieve basement depths. Where the grids  
176 overlap near the ice shelf edge, we retain our RIS values. To aid in the merging at the  
177 overlaps, and to match RIS basement wavelengths to the characteristic basement  
178 wavelengths of ANTOSTRAT, we filtered the merged grid with an 80 km Gaussian filter  
179 (Figure 3a). This filtering was performed with a variety of wavelengths (20-120 km),  
180 where we found filters < 80 km didn't significantly alter the regional basement, while  
181 filters > 80 km excessively smoothed the basement topography. A few locations with  
182 anomalously shallow basement were set equal to BedMachine bathymetry.

183 **Text S6. Sediment thickness and  $\beta$ -factor calculations**

184 With the regional basement model (Figure 3a) including RIS magnetic basement  
185 and offshore seismic basement, we calculated sediment thickness (Figure 3b) by  
186 subtracting the grid from Bedmachine bathymetry depths (Figure 1a & S1e, Morlighem et  
187 al. 2020). Previous estimates of sediment thickness for the sub-RIS come from the  
188 extrapolation of gravity anomalies with bathymetry trends (Wilson and Luyendyk, 2009).  
189 These were included in the Lindeque et al. (2016) compilation (Figure S1d). Eocene-  
190 Oligocene boundary paleotopographic reconstructions (Wilson et al., 2012, Paxman et  
191 al., 2019) assumed this sediment estimate was post-Eocene and used it as their  
192 maximum sub-RIS sediment thickness, incorporated into their minimum surface  
193 reconstruction. The thickness of sediment affects onshore erosion estimates, surface  
194 raising due to deposition, and isostatic surface subsidence due to loading. For their  
195 maximum paleotopographic reconstructions, they used a thinner sediment model, with  
196 the same general trends (Wilson & Luyendyk, 2009). Figure S1 (c, d, & f) shows the  
197 comparison between the sediment thickness models. Figure S1f colorbar histogram  
198 shows the distribution, with our values having a mean thickness ~115m greater than the  
199 past model. Yet, along the Siple Coast, we show much greater discrepancies, up to 2 km  
200 thicker.

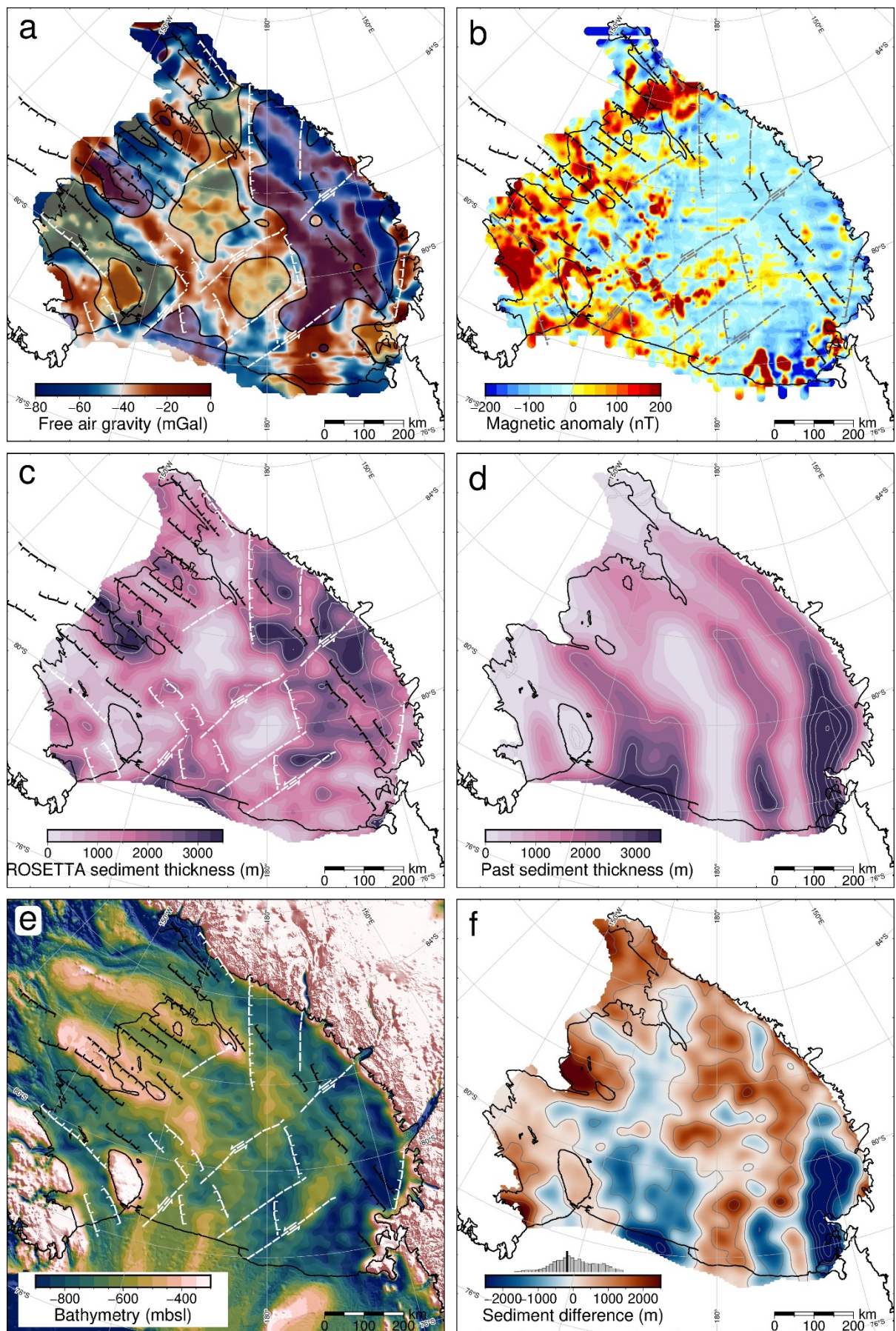
201  $\beta$ -factor, the ratio of initial crustal thickness to final crustal thickness, is useful for  
202 quantifying the thinning of crust in extensional settings. We calculate a distribution of  $\beta$ -  
203 factors beneath the RIS by assuming a uniform initial crustal thickness and dividing it by  
204 current crustal thickness. We pick an initial crustal thickness of 38 km, which represents a  
205 global average for un-thinned plateau-type crust (Mooney et al., 1998), and has been  
206 used for the West Antarctic Rift System  $\beta$ -factor calculations (Müller et al., 2007). For the  
207 final (current) crustal thickness, we use a continent-wide Moho model from surface wave  
208 observations to define the bottom of the crust (An et al., 2015). For the top of the crust,  
209 we use our resulting RIS basement grid.

210 **Text S7. Uncertainties**

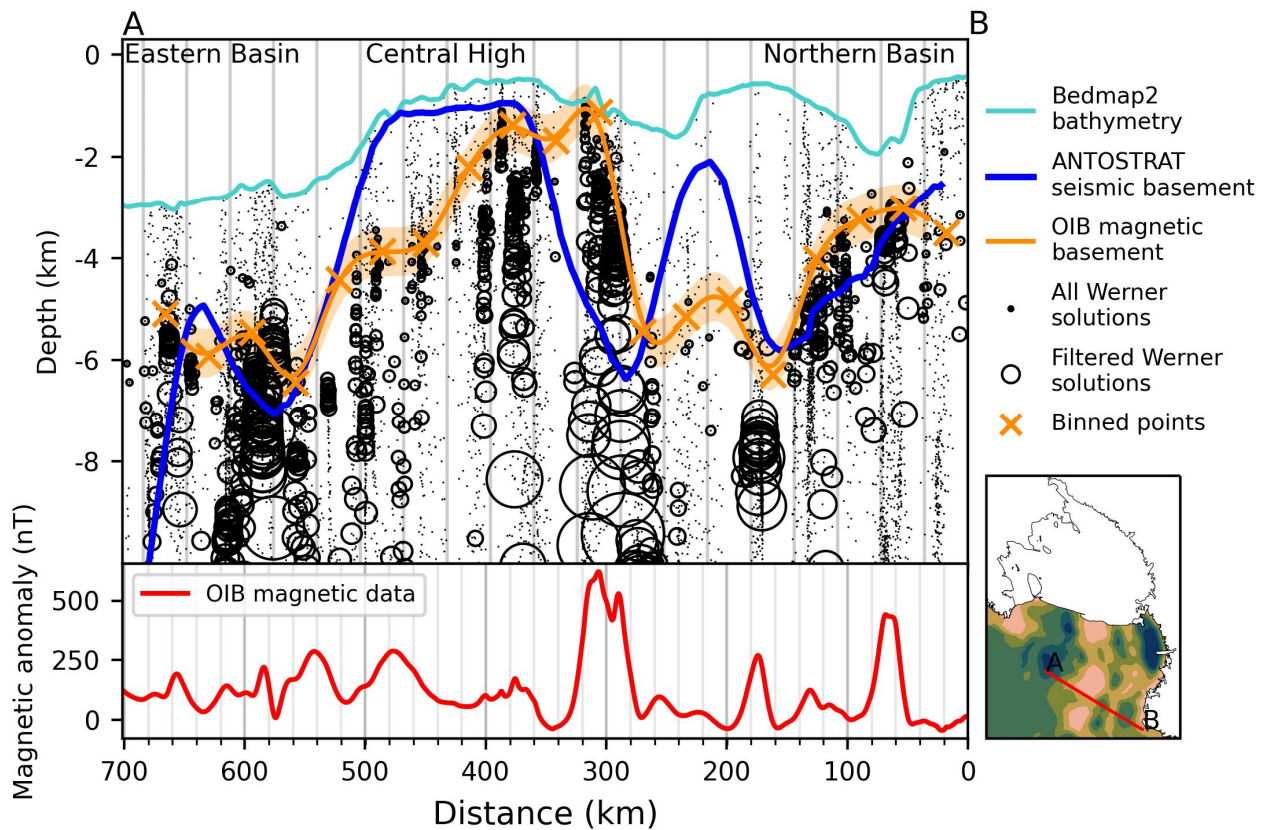
211 We estimated a representative uncertainty for our basement model by examining  
 212 the misfit of our modeled basement compared to offshore seismic basement depths  
 213 (Brancolini et al., 1995). We did this by sampling our OIB magnetic basement estimate  
 214 and the coincident ANTOSTRAT basement at 1 km intervals along lines 403.1 and 403.3  
 215 (Figures 2 and S2) and compared the values. The resulting absolute values of the  
 216 differences don't exhibit a normal distribution (Figure S6a); therefore, we use the median  
 217 of the absolute misfit (+/-480m) as the basement model uncertainty. This equates to  
 218 22% of average basement depths for the sub-RIS. We performed a similar analysis  
 219 between OIB magnetic basement and ROSETTA-Ice magnetic basement for coincident  
 220 lines 590 and 650 (Figure S3 e & f). This resulted in a median absolute misfit of 400m  
 221 (Figure S6b). Tinto et al. (2019) report an uncertainty of 68m for their bathymetry model.  
 222 Incorporating this with our basement model gives an uncertainty of 550m (37% of  
 223 average thickness) for our sediment thickness results. Comparison with sub-RIS sediment  
 224 thickness and distribution results from a variety of methods, including active source  
 225 seismic surveys (Table S1 and references within), seismic radial anisotropy (Zhou et al.,  
 226 2022), geophysical machine learning (Li et al. 2021), and magnetotelluric surveying  
 227 (Gustafson et al. 2022, in review), all show general agreement with our results.

Name	Reference	Seismic sediment thickness (m)	Magnetic sediment thickness (m)	Absolute difference (m)
CIR	Rooney et al. (1987)	400	514	114
I10S	Robertson and Bentley (1989)	750+/-100	1281	818
J9DC	Greischar et al. (1992)	1350	770	580
BC	Robertson and Bentley (1989)	1900+/-400	1082	818
RI	Greischar et al. (1992)	850	822	28
C49	Crary (1961)	754	1162	408
LAS	Crary (1961)	1325	1799	474
Q13	Greischar et al. (1992)	255+/-145	721	466

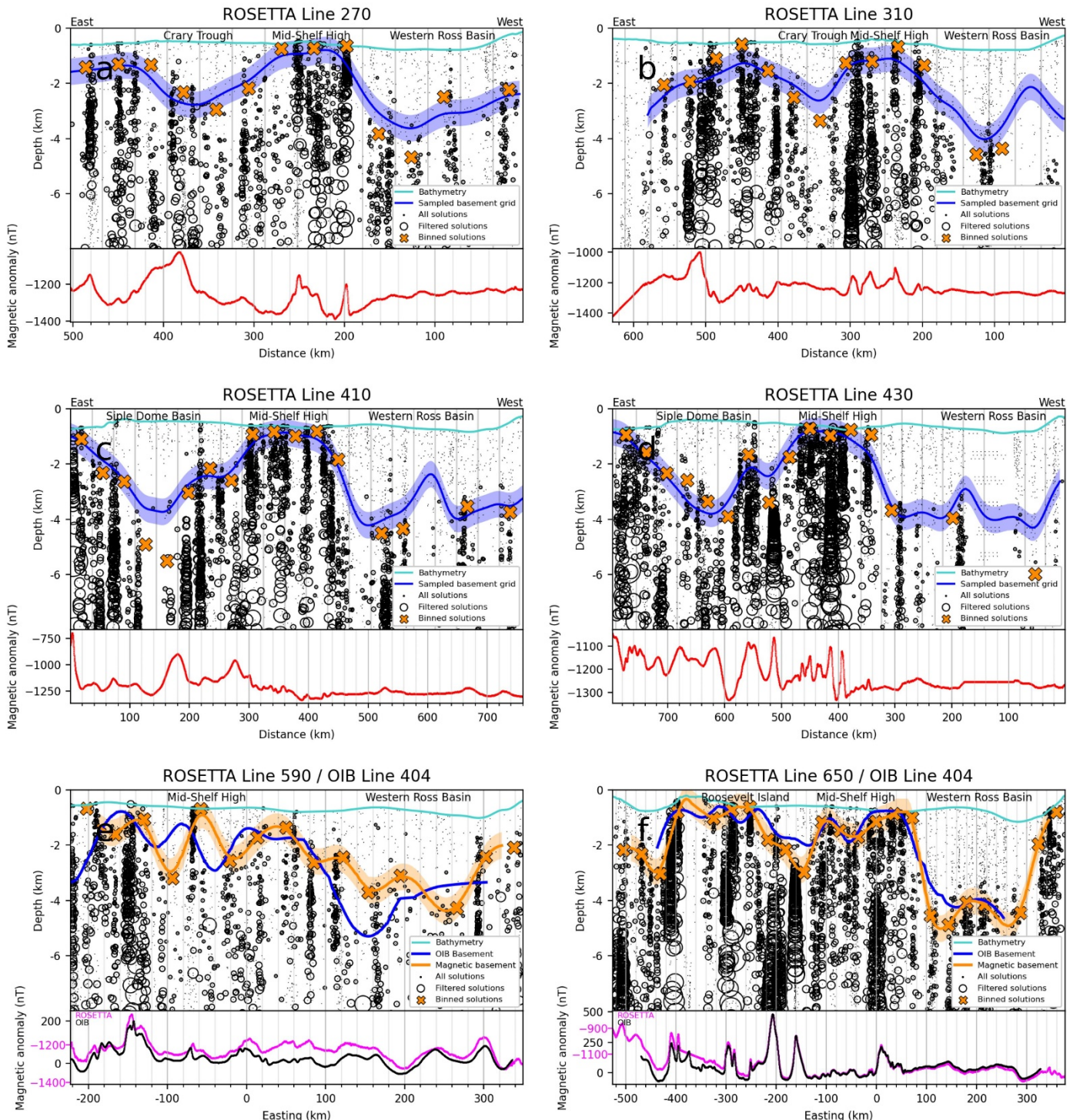
228 **Table S1.** Previous seismic sediment thickness results for the Ross Ice Shelf. Stations  
 229 names are labeled in Figure 3b. Magnetic sediment thickness column shows our sampled  
 230 results at the location of each station. Comparing the seismic estimates with our  
 231 sediment thickness at the eight stations gives a median absolute misfit of 470m.



232 **Figure S1.** (a) ROSETTA-Ice free air gravity (Tinto et al., 2019). Shaded yellow regions are  
 233 shallow basement ( $<\sim 1600$  mbsl), shaded blue regions are deep basement ( $>\sim 2600$   
 234 mbsl). (b) ROSETTA-Ice airborne magnetic anomaly data (Tinto et al., 2019). (c)  
 235 Sediment thickness from this study (same as Figure 3b), with 1 km contours. (d)  
 236 Sediment thickness from a regional compilation (Text S6, Lindeque et al., 2016, Wilson &  
 237 Luyendyk, 2009), with 1 km contours. (e) Bedmachine2 bathymetry (Morlighem et al.,  
 238 2020), from which sediment thickness in (c) was calculated. (f) Difference between (c)  
 239 and (d). Red signifies our results have more sediment, while blue signifies our results  
 240 have less sediment. Histogram shows data distribution, with mean value (black) at 115m.  
 241 Inferred faults in a),b),c), and e) same as Figure 4a. Grounding line and coastlines in black  
 242 (Rignot et al., 2013). Projection is Antarctic Polar Stereographic: EPSG 3031.

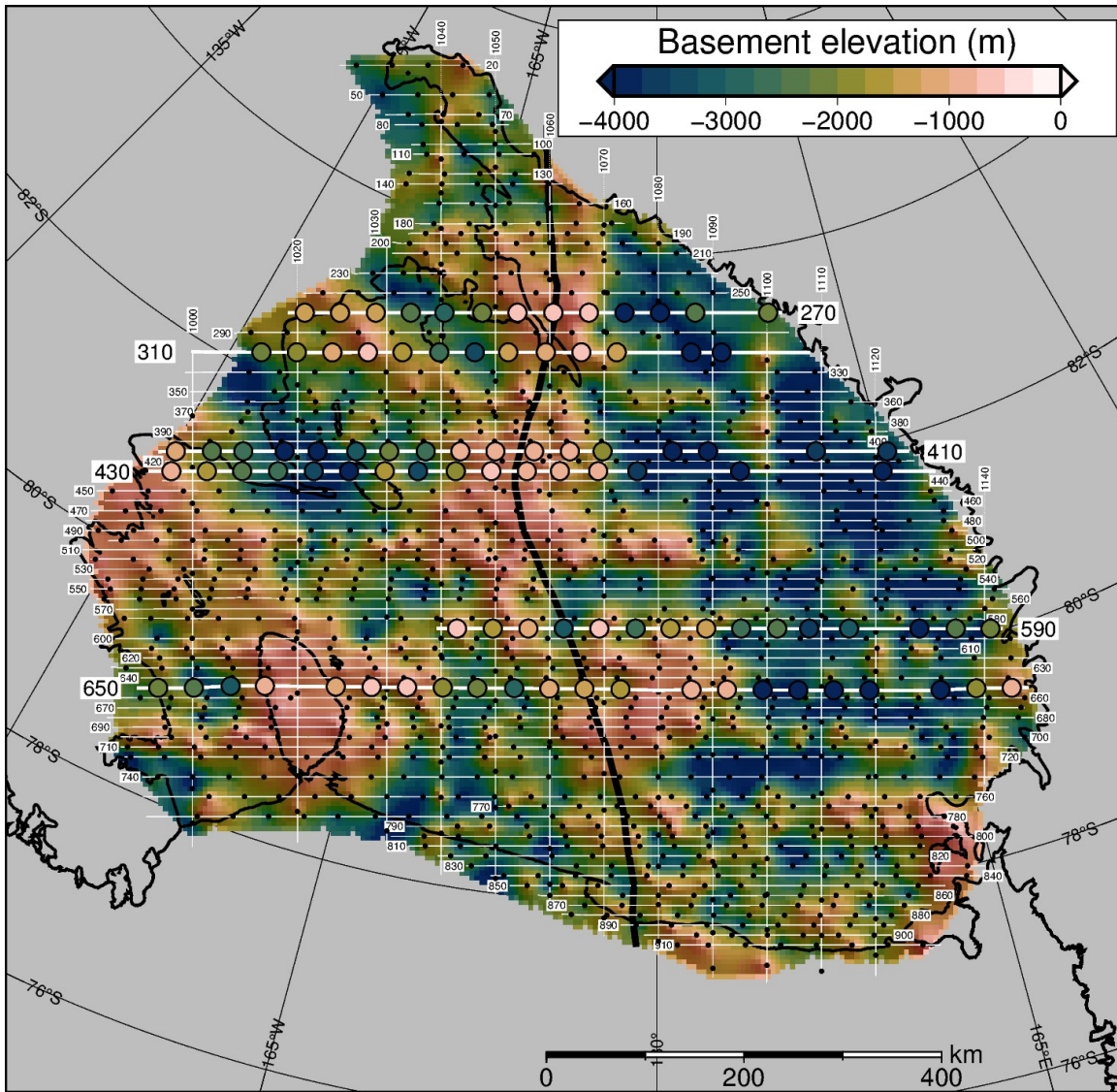


243 **Figure S2.** Ross Sea magnetic and seismic basement comparison. Operation IceBridge  
 244 airborne magnetic data (lower panel) from segment 403.3 (Figure 1b). Small dots show  
 245 Werner deconvolution solutions, which were filtered based on parameter S and W (Text  
 246 S2) to produce black circles, which are scaled to parameter S. These circles were binned  
 247 at a width equal to parameter B, shown by the vertical grey lines in the upper panel.  
 248 Orange crosses show bin centers, which were fitted to a line to facilitate the comparison  
 249 between the magnetic basement (orange line) and seismic basement (blue line). Orange  
 250 band shows  $\pm 480$ m uncertainty for the basement model. Ross Sea basement features  
 251 are labeled on top.

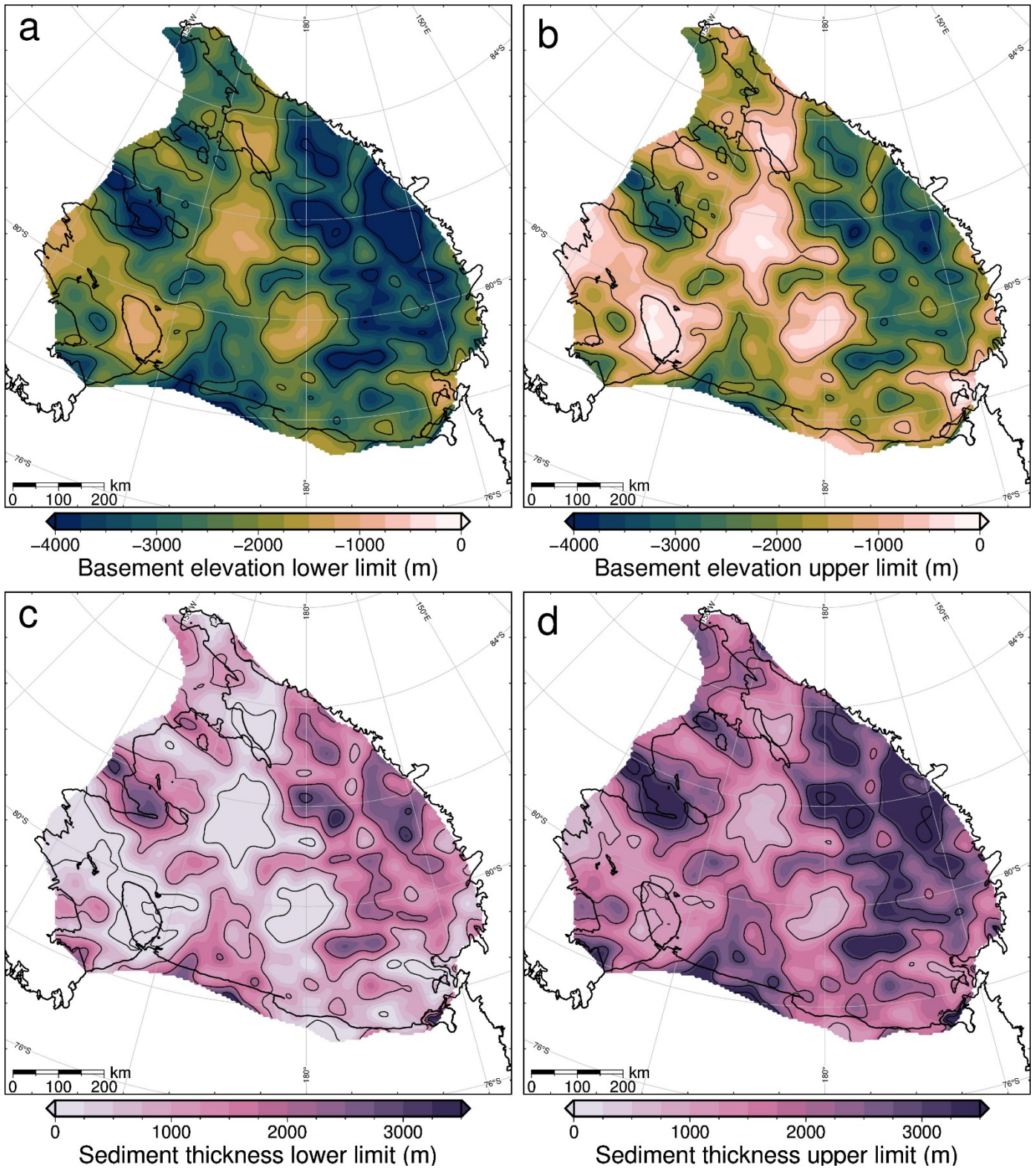


252 **Figure S3.** Werner deconvolution solutions for a selection of ROSETTA-Ice lines,  
253 locations highlighted in Figure S4. Bathymetry from Bedmap2 (Fretwell et al., 2013). Dots,  
254 circles, and vertical grey lines same as Figure S2. **a-d)** Comparison between magnetic  
255 basement before and after filtering and gridding. Orange crosses are magnetic basement  
256 solutions, shown as black dots in Figure S4, and highlighted for these lines. Orange line  
257 with uncertainty bounds is fitted to these solutions. Blue lines are magnetic basement

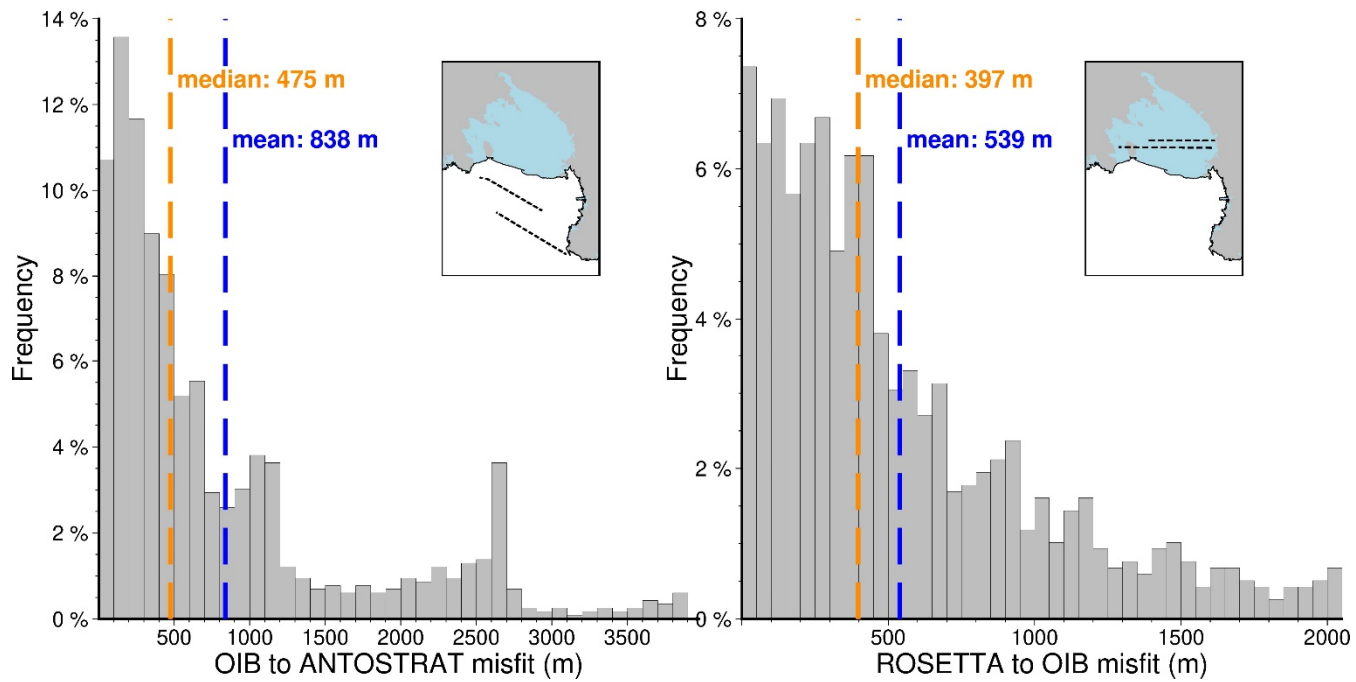
sampled from the grid of Figure 1a, after gridding and filtering. Red lines show ROSETTA-Ice magnetics data. **e-f**) Comparison between magnetic basement resulting from Werner deconvolution of coincident OIB and ROSETTA-Ice flight lines. Location is shown in Figures 1b and S4. These two lines were used to tie the ROSETTA-Ice survey to the OIB survey (Text S4). Blue lines are OIB magnetic basement results, orange crosses and fitted orange lines with uncertainty bands are ROSETTA-Ice magnetic basement. ROSETTA-Ice (pink) and OIB (black) magnetics data are shown in lower panels.



**Figure S4.** Unfiltered magnetic basement. Point solutions (black dots here, orange crosses in Figure S3) along ROSETTA-Ice flight lines (labeled) were gridded with a 5km cell size and a minimum curvature spline with a tension factor of 0.35. Figure S3 flight lines (bold white) and point solutions (colored circles) are shown. Black line through the Mid-Shelf High shows the East-West Antarctic divide used in colorbar histograms of Figures 3 and 4a. Grounding line and coastlines in black (Rignot et al., 2013).



271   **Figure S5.** Upper and lower limits of uncertainty applied to **a-b)** magnetic basement and  
 272   **c-d)** sediment thickness. See Text S7 for how these uncertainties were determined.



273 **Figure S6.** Misfit distributions for comparisons between **a)** OIB magnetic basement and  
 274 ANTOSTRAT seismic basement and between **b)** ROSETTA magnetic basement and OIB  
 275 magnetic basement. Inset maps show locations of flight lines. Basement models were  
 276 sampled at 1km intervals for the comparison.